Africa's Crustal Architecture Inferred from Probabilistic and Perturbational Inversion of Ambient Noise: ADAMA

Tolulope Olugboji[1], **Siyu Xue**[1,2], **Jean-Joel Legre**[1], **Yuri Tamama**[1,3,4]

[1]Department of Earth and Environmental Sciences, University of Rochester, Rochester, NY, USA
[2]Georgen Institute of Data Sciences, University of Rochester, Rochester, NY, USA
[3]Department of Geosciences, Princeton University, Princeton, NJ, USA
[4]Seismological Laboratory, California Institute of Technology, Pasadena, CA, USA

Key Points:

- A continent-wide s-velocity model of Africa's crust is constructed using the largest catalog of dispersion measurements
- The model of Africa's crust is derived from dispersion maps and error statistics obtained from a probabilistic inverse approach
- Error statistics provide insights into the resolution and statistical significance of the final model update.

Corresponding author: Tolulope Olugboji, `tolugboj@ur.rochester.edu`

Abstract

Africa's continental crust hosts a variety of geologic terrains and is crucial for understanding the evolution of its longest-lived cratons. However, few of its seismic models are yet to incorporate the largest continent-wide noise dispersion datasets collected on the continent. Here, we report on new insights into Africa's crustal architecture obtained using a new dataset and model assessment product, ADAMA, which comprises a large ensemble of short period surface wave dispersion measurements. We construct a continent-wide model of Africa's Crust Evaluated with ADAMA's Rayleigh Phase maps (ACE-ADAMA-RP). Phase and group dispersion maps are obtained with a probabilistic inverse modeling approach allowing us to provide constraints on uncertainty. Error statistics suggest Rayleigh phase maps are better resolved and a perturbational inverse approach based on Rayleigh waves is the basis of our update of Africa's crustal shear velocity. This model update reveals new insights into the architecture of Africa's crust not previously imaged: (1) the fastest velocities confined to the edges of the Congo craton, the west-African cratons and the Sahara Metacraton, and (2) sharp spatial gradients along craton edges, mobile belts, and within rifted margins. While most of the reported features are robust, probabilistic modeling suggests caution in interpreting features where illumination is compromised by low-quality measurements, sparse coverage or both. Future extension of our approach to other complementary seismic and geophysical datasets - e.g, multimode earthquake dispersion, receiver functions, gravity and mineral physics, will enable continent-wide lithospheric modeling that extends resolution to the upper mantle.

Plain Language Summary

The rocks that constitute Africa's crust record the history of different geological periods. We produce a map, for the entire continent, of how fast shear waves travel within these rocks. We obtain this map from ambient noise surface wave vibrations. The ambient noise surface waves are generated from ocean and atmospheric waves that couple with the solid Earth. There are two types: Rayleigh and Love waves and they travel at different speeds for different wavelengths. This property is called dispersion and it is used to tell how fast the shear wave speeds travel within the subsurface rocks. Constructing the final map from ambient noise surface waves requires the solution of a computational imaging problem. We solve the most challenging computational task with a probabilistic approach – using random sampling – and this enables us to also construct associated error maps. The new maps of Africa's crust show new features that have important implications for subsurface geology of the continent.

1 Introduction

The African continent possesses many geological terrains and tectonic features of great interest, including multiple cratons spanning billions of years in age (Begg et al., 2009; Jessell et al., 2016), a long-wavelength superswell topography in the south (Lithgow-Bertelloni & Silver, 1998; Fishwick & Bastow, 2011), active and failed continental rifts (Chorowicz, 2005; Min & Hou, 2019), hotspots and active volcanoes and multiple second-order basins and swells (Doucouré & de Wit, 2003; Burke & Gunnell, 2008)(Figure 1a). One approach to studying the diverse and spatially undersampled regions of Africa's bulk crust is to turn to seismic velocity models (Adams & Nyblade, 2011; Pasyanos et al., 2014; Emry et al., 2019). These models provide useful constraints on the composition of the crust (Hacker et al., 2012; Rudnick & Gao, 2014; Sammon et al., 2021), the identification of structural boundaries within and across different tectonic domains (Buehler & Shearer, 2017) and how rheology (Shinevar et al., 2015, 2018) and density (Molinari & Morelli, 2011; Haas et al., 2020, 2021) influence continental rifting, isostatic and dynamic uplift, long-term deformation, and seismicity within the African plate (Behn et al., 2002; Lowry & Pérez-

Gussinyé, 2011; Schmandt et al., 2015; Borrego et al., 2018; Schutt et al., 2018; Fadel et al., 2020; White-Gaynor et al., 2021).

Insight into Africa's crust is provided by global (Laske et al., 2013; Pasyanos et al., 2014), as well as continent-wide velocity models (Li & Burke, 2006; Nair et al., 2006; Yang et al., 2008; Begg et al., 2009; Adams & Nyblade, 2011; Fishwick & Bastow, 2011; Fadel et al., 2020). A selection of the continent-wide seismic velocity models published in the last decade include Litho1.0 ((Laske et al., 2013; Pasyanos et al., 2014), Africa.ANT.Emry-etal.2018 (Trabant et al., 2012; Emry et al., 2019), AF2019 (Celli, Lebedev, Schaeffer, & Gaina, 2020), and SA2019 (Celli, Lebedev, Schaeffer, Ravenna, & Gaina, 2020). All of these models are replicas of CRUST1.0 (Laske et al., 2013; Pasyanos et al., 2014) in the shallowest crust, except for Litho1.0, a heavily cited global velocity model, which updates CRUST1.0 by incorporating earthquake-derived surface wave dispersion measurements, independent constraints sensitive to elastic properties in the lithosphere (Laske et al., 2013; Pasyanos et al., 2014). Taken together, these models incorporate both active and passive source datasets, but are yet to fully integrate comprehensive ambient noise data on the continent (T. Olugboji & Xue, 2022).

As a result, these models are limited in their resolution of Africa's crust in two key respects. First, because they do not include shortest period measurements, they lack sensitivity to absolute velocity in the shallowest crust (Roux et al., 2005; Yang et al., 2008). Second, because the continent-wide models do not include all seismic data acquisition spanning the past decade (2013-2023), (Accardo et al., 2017; Borrego et al., 2018; Emry et al., 2019; Wang et al., 2019; Fadel et al., 2020; Celli, Lebedev, Schaeffer, & Gaina, 2020; White-Gaynor et al., 2021), they lack spatial resolution across key tectonic domains. Here, we address this and other key issues necessary for building an updated model of Africa's crust using the ambient noise dataset and model assessment product (ADAMA), provided by (T. Olugboji & Xue, 2022). We use these measurements to construct continent-wide Love and Rayleigh wave dispersion maps using a probabilistic approach. The inclusion of short-period surface wave measurements provides improved constraints on short-wavelength features, especially at the shortest periods (Lebedev et al., 2013). This allows us to provide greater resolution of the shallowest crust (Figure 1b & 2a).

In constructing new dispersion maps, we adopt a probabilistic Bayesian approach that solves for an image of surface wave speeds in the presence of irregular ray path coverage and variable measurement quality (Bodin et al., 2009; Bodin, Sambridge, Tkalčić, et al., 2012; Bodin & Sambridge, 2009; Bodin, Sambridge, Rawlinson, & Arroucau, 2012; T. M. Olugboji et al., 2017). This technique is well suited to the dataset obtained from Africa. Furthermore, it also provides information on statistical significance - that is, associated maps that quantify uncertainties in the final reported dispersion maps (Bodin, Sambridge, Tkalčić, et al., 2012; T. M. Olugboji et al., 2017). The dispersion maps with associated uncertainties are a useful data product since they span the entire continent and can be used to assess (T. M. Olugboji et al., 2017) and update existing models during linear and non-linear inversions for elastic properties in the crust (Shen & Ritzwoller, 2016; Shen et al., 2016).

In the rest of our paper we describe, in detail, the construction of our new maps, highlighting key benefits of adopting a probabilistic Bayesian approach. We present details, not yet seen before, with illumination made possible by the comprehensive ADAMA dataset. We investigate the statistics and resolution present in the maps using the ensemble results obtained from sampling the posterior distribution, comparing our results to existing published results at similar periods. We provide an assessment of one of the global velocity models, Litho1.0, by inverting the phase maps for depth dependent shear-wave velocity structure in Africa's crust. We discuss implications of our model for unanswered questions in Africa's tectonics and basement geology.

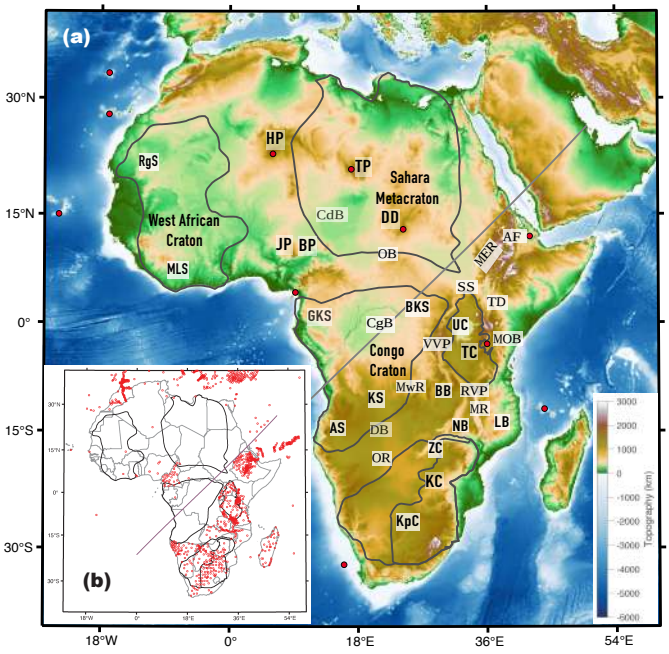

Figure 1. A broad view of Africa's geology overlaid on topography (a) The key geological tectonic features are: cratons and metacratons (gray outline), basins (low topography), hotspots (red dots). Craton outlines are from (Globig et al. 2016; Afonso et al. 2022). Abbreviations are: AF = Afar; AS = Angolan Shield; BB = Bengweulu Block; BKS = Bomu-Kibalan Shield; BP = Biu Plateau; CdB = Chad Basin; CgB = Congo Basin; CVL = Cameroon Volcanic Line; DB = Damara Belt; DD = Darfur Dome; GA = Gulf of Aden; GKS = Gabon-Kamerun Shield; HP = Hoggar Plateau; JP = Jos Plateau; KC = Kalahari Craton; KpC = Kaapvaal Craton; KS = Kasai Shield; LB = Lurio Block; MOB = Mozambique Orogenic Belt; MER = Main Ethiopian Rift; MLS = Man-Leo Shield; MR = Malawi Rift; MwR = Mweru Rift; NB = Niassa Block; OB = Oubanguides Belt; OR = Okavango Rift; Rgs = Reguibat Shield; RS = Red Sea; RVP = Rungwe Volcanic Province; SS = South Sudan; TC = Tanzania Craton; TD = Turkana Depression; TP = Tibesti Plateau; UC = Uganda Craton; VVP = Virunga Volcanic Province; ZC = Zimbabwe Craton. (b: Inset): Station distribution (red dots) used to obtain ADAMA dispersion dataset (T. Olugboji Xue 2022). Transect passing through the Congo craton and Ethiopian highlands is used to produce a 2-D vertical slice of the final crustal shear-wave velocity model after ADAMA update (see Figures 7 & 9) .

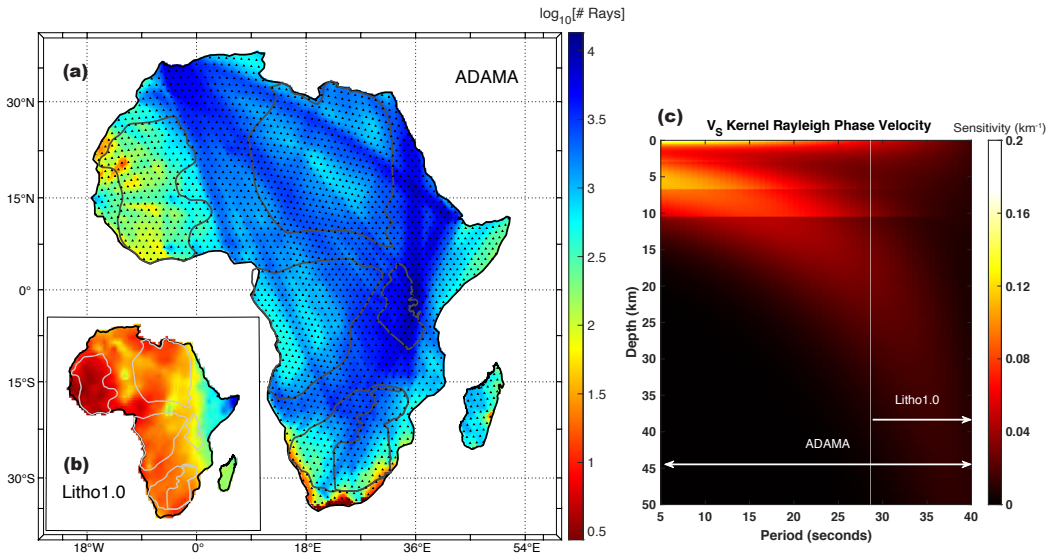

Figure 2. Shear wave sensitivity to Spatial coverage and Rayleigh wave for the ADAMA dataset. (a & b) Raypath density for the ADAMA dataset compared to a global model published in 2014 (Pasyanos et al. 2014). (c) Improved depth-sensitivity of ADAMA compared to the global Litho1.0 model showing improvements from short-period measurements.

2 Continent-wide Ambient Noise Dataset from ADAMA

The dataset used in this study - ADAMA - is from the recently published catalog of continent-wide inter-station dispersion measurements provided by (T. Olugboji & Xue, 2022). This is a large catalog of Love and Rayleigh wave phase and group dispersion measurements. The dispersion measurements are extracted from cross-spectra of continuous recordings of ambient noise ground vibrations, collected over four decades, since the commencement of digital seismometry on the continent. The inter-station cross-spectra are calculated from seismograms downloaded from 1,372 stations, spanning 62 networks in and across Africa (e.g., southern Europe, and the Middle East). The dataset spans a large collection of inter-station ray paths that provide improved spatial coverage and depth resolution of the entire continent (Figure 1b & 2a).

2.1 Love and Rayleigh Waves Dispersion with Uncertainties

For each station pair, phase and group velocities of Love and Rayleigh waves between 5 and 40 seconds are reported. Measurement uncertainty is also reported using a non-linear waveform fitting of the ambient noise cross-spectra, providing necessary regularization information during probabilistic inversion of our maps (Hawkins & Sambridge, 2019). For a detailed description of the dataset catalog, we refer the reader to (T. Olugboji & Xue, 2022). Here, we describe how improved spatial coverage and short-period measurements provide improved resolution of the crust. We also show how the entire catalog of inter-station dispersion measurements are used to obtain dispersion maps, uncertainties and shear-velocity in the entire crust.

2.2 Ray Coverage and Depth Sensitivity to Crustal Structure

The ADAMA dataset improves on global and regional surface wave dispersion catalogs in two regards: the first is increased ray-path density with better spatial sampling across the entire continent and second is that it extends the surface wave dispersion measurements to very short periods (< 25 seconds). At the shortest periods, and with rays sampling the entire continent, good resolution of the crust across the entire continent is possible (Figure 2). The new dataset reflects three orders of magnitude more measurements than the most recent continent-wide study (Emry et al., 2019).

3 Methods

3.1 Auto Adaptive & Probabilistic Noise Maps for Model Update of Africa's Crust

We construct dispersion maps by employing a probabilistic inverse approach. This approach solves for the spatial distribution of phase and group speeds, with associated uncertainties, while imposing minimal restrictions on parameterization and regularization. In Africa, where spatial sampling is highly irregular, and crustal structure is irregular, an optimal parameterization along with modeling uncertainties can still be recovered during tomographic inversion. The technique is known as transdimensional hierarchical Bayesian inversion (THBI), and has been widely used by many authors to construct surface wave dispersion maps (see (Zulfakriza et al., 2014; Galetti et al., 2016; Rawlinson et al., 2016; Crowder et al., 2019; Pilia et al., 2020). A comprehensive discussion of THBI can be found in (Bodin et al., 2009; Bodin, Sambridge, Rawlinson, & Arroucau, 2012; Bodin, Sambridge, Tkalčić, et al., 2012). Here we provide a brief overview of the approach, show how we apply it to the ADAMA dataset, and describe how we use the maps themselves for model assessment and update of the African crust, following the statistical approach of (T. M. Olugboji et al., 2017). We do this by demonstrating that our new maps, constructed with THBI, contain information across multiple scales not yet incorporated into the continent-wide models (Pasyanos et al., 2014; Wipperfurth et al., 2020; Sammon et al., 2021). We compare model predictions of dispersion with our new probabilistic maps. Tests of statistical significance and evaluation of improved resolution are estimated using ensemble statistics. In regions of improved spatial coverage and where model predictions are different from data (dispersion maps), updates to crustal structure are obtained. We report updates, in these regions, using a perturbational inversion of our new dispersion dataset (Haney & Tsai, 2017, 2020).

3.2 Noise Maps with Transdimension Hierarchical Bayesian Inversion

The transdimensional and hierarchical Bayesian inverse approach is a class of sampling methods that seeks not just a single optimal model (dispersion maps), but rather searches the parameter space for all possible model solutions that best satisfy the observational constraints (interstation dispersion measurements). The interpretation of the ensemble of model solutions is then used to evaluate formal uncertainty. In this approach Bayesian statistics is applied to the twin challenges of model regularization and non-uniqueness. In the first part of the inversion, the transdimensional inference recognizes that the initial step of image reconstruction requires the parameterization of a 2-D surface velocity field, $\mathbf{V}(\mathbf{r})$ and this is specified by a variable number of basis (descriptor) functions and values, which are unknowns to be specified as part of the inverse solution:

$$\mathbf{V}(\mathbf{r}) = \sum_{i}^{N_i} v_i \mathbf{I_i} \tag{1}$$

Where the N_i velocity values, v_i, sampled at points $\mathbf{r_i}$ are allowed to vary across the 2-D surface, thus ensuring that the velocity field is adaptively parametrized. In our imple-

mentation, we use a nearest-neighbor Voronoi tessellation (Figure 3a) as the basis function $\mathbf{I_i}$ (Sambridge et al., 1995). This function tessellates the velocity field, $\mathbf{V}(\mathbf{r})$, and is widely used in transdimensional inversion (Bodin et al., 2009; Bodin, Sambridge, Rawlinson, & Arroucau, 2012); although we note here that other forms of tessellations have recently been advocated (Belhadj et al., 2018; Hawkins et al., 2019) with beneficial properties like smoothness.

In the second part of the inversion, the hierarchical inference recognizes that all inverse problems are fraught with uncertainty. That is, given the data vector of observations, $\boldsymbol{d}$, and the model parameters m= $\left\{\mathrm{v}_i, r_i, N_i\right\}$ representing our 2-D image of the earth, errors are expected:

$$g(\mathbf{m}) = \mathbf{d} + \epsilon \tag{2}$$

The errors, $\epsilon = \epsilon_{data} + \epsilon_{theory} + \epsilon + \ldots$, can either be due to: (1) simplifying assumptions posed by our forward modeling operator $g(\mathbf{m})$ (e.g., in our case using ray theory (Shen & Ritzwoller, 2016) instead of eikonal tomography (Lin et al., 2009; Zhou et al., 2012)), (2) observational noise which cannot be modeled even in the case of a true model $g(\mathbf{m}_{true})$, or (3) sampling and discretization errors introduced from an approximate parameterization as described in Equation 1 above. Within the Bayesian framework, the likelihood of a particular set of model predictions, are those that minimizes the probability on the prediction error term, and by definition maximizes the gaussian likelihood:

$$p(\mathbf{d}|\mathbf{m}) = \frac{1}{\prod_j \sqrt{2\pi\sigma_j}} \exp\left(-\sum_j \frac{(g(\mathbf{m})_j - \mathbf{d}_j)^2}{2\sigma_j^2}\right) \tag{3}$$

The standard deviation term, σ, is the hierarchical parameter, and is an additional model parameter to be solved for in the hierarchical Bayes (Malinverno & Briggs, 2004) inversion. But note that it is defined in a way so as to represent all of the sources of error present in modeling and observation, so: $\sigma_i = \sigma_{i,data} + \sigma_{theory}$. Admittedly this is a rather simplistic model, since we do not investigate covariation in measurement errors. Nonetheless, by solving for a single scaling parameter for each period, we can accommodate for this, so that:

$$\sigma_i = \lambda\sigma_{i,data} \tag{4}$$

In summary, a transdimensional and hierarchical Bayesian inverse solution of our noise dispersion measurements produces dispersion maps that involves sampling the posterior probability distribution for a collection of extended set of model parameters:

$$\mathbf{X} = \{\mathbf{m}, \lambda\} = \{v_i, r_i, N_i, \lambda\} \tag{5}$$

$$P(\mathbf{X}|\mathbf{d}_j = t_j^{c,u}) \propto P(\mathbf{d}_j = t_j^{c,u}|\mathbf{X})p(\mathbf{X})(\tag{6}$$

Where $p(\mathbf{X})$ and $P(\mathbf{d_j} = t_j^{c,u}|\mathbf{X})$ are the prior and likelihood on the extended set of model parameters $\mathbf{X}$ (actual model parameterization, $\mathbf{m}$, and hierarchical uncertainties λ), $\mathbf{d_j}$ is the data (dispersion measurements), N_j is the number of inter-station travel time measurements, for station separation, r_j, using either the interstation phase velocity, c_j or group velocity, u_j: $t_j^c = c_j/r_j; t_j^u = u_j/r_j$. The prior distribution is a uniform distribution,

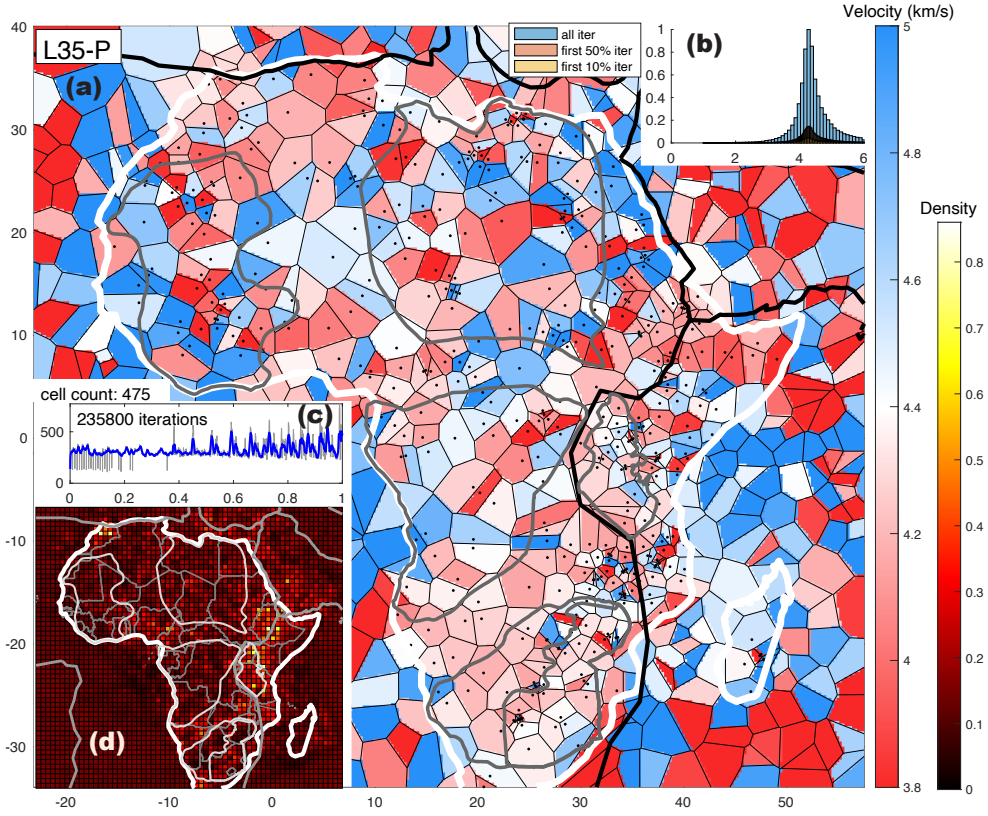

Figure 3. A snapshot through the Transdimensional Hierarchical Bayesian Inversion algorithm. (a) A single snapshot of model,**m**, showing the irregular Voronoi tessellation used to parameterize the Love wave 2-D phase velocity map at 35 seconds. The velocity values are constant within each cell and the node centers are irregularly located in the domain (black dots). (b) The posterior distribution of the phase velocity map (blue) and after discarding the first 10% or 50% or the samples (c) A time-series tracking the total number of Voronoi cells across all parallel chains in the Monte Carlo random walk. (d) A similar statistical analysis but showing the Voronoi cell density (number of cells per pixel) across all the chains.

	Variable	Description
	I. *Bayesian Probabilistic Framework*	
1	$P(\mathbf{X}\|\mathbf{d}_j = t_j^{c,u})$	Posterior distribution on model parameters $\mathbf{X}$, given data, $\mathbf{d}$
2	$p(\mathbf{X})$	Prior distribution on model parameters $\mathbf{X}$
3	$P(\mathbf{d_j} = t_j^{c,u}\|\mathbf{X})$	Likelihood of data, $\mathbf{d}$, given model $\mathbf{X}$
4	$t_j^{c,u}$	Inter-station travel time measurements
	II. *Transdimensional and Hierarchical Model Definition*	
5	$\mathbf{X_k} = \{\mathbf{m_k}, \lambda_k\}$	A set of $3N_i + 2$ parameters for every k_{th} McMC step
6	$\mathbf{m_k} = \{v_{ik}, r_{ik}, N_{ik}\}$	The transdimensional model parameters
7	$\mathbf{V(r)}$	The Voronoi tessellation for a 2-D velocity field
8	$\mathbf{I}$	Interpolating function that uses the Voronoi nodes
9	N_i	number of Voronoi nodes
10	λ_k	observational error for each map
11	v_{ik}^p	Phase velocities at N_i nodes
12	v_{ik}^g	Group velocities at N_i nodes
13	$\mathbf{r}_{ik} = (\theta_{ik}, \phi_{ik})$	location (longitude, latitude) of the center Voronoi nodes
	III. *Forward Problem and Observational Data*	
14	$g(\mathbf{m})$	Forward problem predicts data given model $\mathbf{X}$ (great circle, bezier, fast marching, etc..)
15	N_j	number of available interstation phase dispersion measurements
16	$\mathbf{d}_j = t_j^{c,u}$	data is N_j travel-time observations
17	c_j	phase dispersion measurement for stations i, j
18	u_j	group dispersion measurement for stations i, j
19	r_j	Interstation distance
	IV. *McMC Sampling Strategy*	
20	N_c	Number of chains run in parallel
21	N_k	Number of Monte Carlo (McMC) steps per chain
22	b	No of burnin steps discarded before averaging
23	Δ_k	length of thinning steps ensures decorrelation during averaging

Table 1. A list of variables and definitions used in describing the transdimensional and hierarchical Bayesian inverse formulation

$p(\mathbf{X}) = \frac{1}{\beta - \alpha}$, on the set of model parameters, $\mathbf{X}$ (in Equation 5) and is specified by identifying the lower and upper limits (α, β). For a summary of the most relevant parameters in the THBI process see Table 1.

The solution to $\mathbf{X}$ is found by sampling the posterior distribution in Equation 6 using a reversible-jump Markov chain Monte Carlo (rj-McMC) algorithm (Green 1995). The algorithm proceeds through a random walk by perturbing an initial model $\mathbf{X}$ to give $\mathbf{X}'$ on every step, adding $\mathbf{X}'$ to a collection of likely models and setting $\mathbf{X}'$ back to $\mathbf{X}$ if the model is accepted. Accepting (or rejecting) a proposed model is governed by acceptance probabilities that are defined in order to allow efficient sampling of the posterior distribution, and include models that, in the long run, increase the likelihood ratio of new proposed models. In this

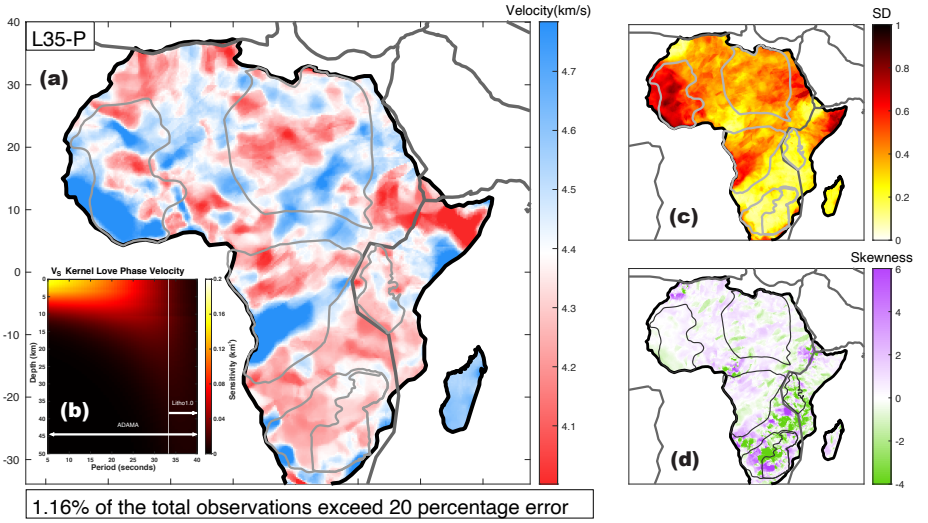

Figure 4. Statistical estimators of the posterior distribution on the 30s-Love wave phase map. (a) The mean dispersion map. (b) The sensitivity of Love waves to shear-wave velocity. (c) The standard deviation of the phase map provides an estimate of uncertainty in the phase map shown in (a) as reconstructed during the sampling of the posterior distribution. (d) A second estimator of the statistics of the posterior distribution, the skewness (second-moment) of the probability distribution showing deviation from non-gaussian statistics.

description, we leave the details of acceptance probabilities to the following papers for a complete discussion (Bodin et al., 2009; Hawkins et al., 2019). We point out that in the reversible jump transdimensional step, the number of model parameters, that is the set $\mathbf{m} = \{v_i, r_i, N_i\}$, is allowed to grow or shrink on every rjMcMC step. These steps are often referred to as the birth and death steps. They represent two of the four perturbation states when going from $\mathbf{X}$ to $\mathbf{X}'$ (Figures 3b-d). The other two perturbation states involve changing the velocity values, v_i or the hierarchical noise parameter, λ. Therefore, given a collection of N_k steps, sampled over N_c parallel chains, we obtain a final average phase or group velocity map by using the entire ensemble in $\mathbf{X}_k$ (Figure 4a):

$$\bar{V}^{p,g}(\omega_l, \mathbf{r}) = \int_m \mathbf{m} P(\mathbf{m}) d\mathbf{m} \approx \frac{1}{N_T} \sum_{k=b+\Delta_k}^{k=N_k \times N_c} v_{ik}^{p,g} \mathbf{I}_i(\mathbf{r}_{ik}) \tag{7}$$

Where the equations represents ensemble averaging using the nearest-neighbor tessellation of the Voronoi cells centered at longitude and latitude node coordinates $\mathbf{r}_{ik} = (\theta_{ik}, \phi_{ik})$. Whether a phase or group velocity node is implied: v_{ik}^p, v_{ik}^g, is dependent on which dataset is used, $\mathbf{d_j} = t_j^{c,u}$ (see Equation 6). During ensemble averaging, we use a total of N_T samples, discarding b burnin steps, and downsampling each chain using a thinning parameter Δ_k:

$$N_T = N_c \times \left(\frac{N_k - b}{\Delta_k} \right) \tag{8}$$

We also use the ensemble and its average to compute statistical estimators of the dispersion maps' posterior distribution: that is standard deviation or second moments (skewness) (Figure 4b-c), providing a quantitative measure of statistical significance on each solution

(Bodin et al., 2009; Bodin & Sambridge, 2009; Bodin, Sambridge, Rawlinson, & Arroucau, 2012; T. M. Olugboji et al., 2017):

$$\xi^{p,g}(\omega_l, \mathbf{r}) = \int_m (\mathbf{m} - \bar{\mathbf{m}})^{\mathbf{2}} P(\mathbf{m}) d\mathbf{m} \approx \frac{1}{\sqrt{N_T}} \sum_{k=b+\Delta_k}^{k=N_k \times N_c} \left[v_{ik}^{p,g} \mathbf{I}_i(\mathbf{r}_{ik}) - \bar{V}^{p,g} \right]^2 \tag{9}$$

In one sense, the average dispersion maps are model solutions of an inverse transformation g^{-1} obtained through Monte Carlo Markov chain (McMC) sampling. The McMC sampling transforms the inter-station travel-time observations, N_j data vectors, into N_R dispersion curves: $[\mathbf{d_j} = t] \xrightarrow{g^{-1} \approx P(\mathbf{X})} [\mathbf{d_R} = V^{p,g}]$. The dispersion curve at each point on the African continent can then be used to solve for an earth model, $\mathbf{m}^{\beta,\alpha,\rho}(z)$:

$$\mathbf{f}(\mathbf{m}^{\beta,\alpha,\rho}(z)) = \mathbf{d_R} \tag{10}$$

Where, $\mathbf{f}$ is a non-linear forward model that maps a local 1D earth model into our data of dispersion curves $\mathbf{d_R}$ and α,β are the compressional and shear velocities and ρ is the density, all varying with depth, z. We discuss, next, our approach to obtaining this earth model

3.3 Shear-Velocity Model Assessment and Update using a Perturbation Method

We use the dispersion curves obtained from the phase velocity maps to invert for an updated earth model using a perturbational approach (Haney & Tsai, 2017). We focus on assessing the shear velocity models of the global lithospheric model of (Pasyanos et al., 2014) using the Rayleigh wave dispersion measurements alone, thus highlighting regions with large data misfits. The perturbational approach uses dispersion data obtained from Bayesian inversion to generate an updated model from a starting shear velocity model (e.g., Litho1.0), and uses an iterative gradient descent method to solve the nonlinear forward model (Equation 10) using a modified augmented system of equations:

$$\begin{bmatrix} \mathbf{C_d^{-1/2}G} \\ \mathbf{C_m^{-1/2}I} \end{bmatrix} \mathbf{\Delta m_k^\beta} = \begin{bmatrix} \mathbf{C_d^{-1/2}\Delta d_k} \\ \mathbf{0} \end{bmatrix} \tag{11a}$$

$$\mathbf{F_k \Delta m_k^\beta} = \mathbf{D_k} \tag{11b}$$

b.1: Iterative solution starts with $\mathrm{m}_0^\beta : \mathbf{\Delta d_k} = \mathbf{d_R} - \mathbf{f}(\mathbf{m_k^\beta})$

b.2: Solving: $\Delta m_k^\beta = [\mathbf{F_k^T F_k}]^{-1} \mathbf{F_k^T D_k}$

b.3: Updating: $\mathrm{m}_{k+1}^\beta = \mathbf{m_k^\beta} + \mathbf{\Delta m_k^\beta}$

b.4: Repeating until: $\chi^2 = \frac{\mathbf{D_k^T D_k}}{F} 1 + \epsilon$

Where $\mathbf{m_0^\beta}$ and $\mathbf{\Delta m_k^\beta}$ are the shear wave velocity and its k-th update and $\mathbf{d_R}$ and $\mathbf{\Delta d_k}$ are the observed dispersion curves and the prediction error for each iteration (Equation 10). The stopping criterion is reached (Equation 11b.4) when the dispersion measurements are matched by the predicted data for a given number of measurements, $F = l$ and $\epsilon = 0.5$. The augmented system (Equation 11a) requires computing the sensitivity kernel $\mathbf{G}$, and the data and model covariance matrices, $\mathbf{C_d}$ and $\mathbf{C_m}$:

$$\mathbf{C_d} = \xi^2(\omega)\mathbf{I} \tag{12a}$$

$$\mathbf{C_m} = \gamma\xi^2(\omega)\exp(\frac{-|z_i - z_j|}{d}) \tag{12b}$$

Data covariance is diagonal and prescribed from measurement uncertainties obtained from Bayesian inversion (Equation 9), while the full matrix representing the covariance of model parameters at depth nodes z_i and z_j is prescribed by two user-supplied factors: a smoothing distance or correlation length, d, and a scaling factor γ. These parameters prescribe some type of regularization to the model solution and weight the degree of data.

In model assessment, we constrain shear-wave velocity by assuming (1) that the Poisson ratio and densities of the Litho1.0 model are fixed or (2) compressional velocity and density can be estimated from shear velocity, using scaling relationships derived from empirical measurements of rock elasticities (Brocher, 2005). We then use the Rayleigh wave phase dispersion results, that is the data and uncertainties, as the constraints in producing an updated model of Africa's Crust Evaluated with ADAMA Rayleigh Phase maps (ACE-ADAMA-RP) following the iterative scheme of Equation 11. We point out that this is just one way to use the new ADAMA dataset. In principle, we could produce a new model not tied to any apriori reference model and use all the Surface Wave dispersion maps - Love dispersion as well as Rayleigh and group velocity as well as phase velocities (ACE-ADAMA-SW). Additionally, we could adopt a similar probabilistic approach to jointly invert the surface wave dispersion datasets with other body-wave seismic measurements like receiver functions (Bodin, Sambridge, Tkalčić, et al., 2012). We defer this to future work. Here, we focus on producing a model update (ACE-ADAMA-RP) based on a reference global model (Litho1.0), so that our new dispersion maps can be benchmarked and the updated models can be evaluated in the context of statistics generated from the computationally expensive THBI algorithm.

4 Results

We summarize the THBI solutions using representative Rayleigh and Love wave phase dispersion maps discretely sampled at four periods (8, 15, 20 and 35). The full solution is archived as a digital open source model (see data acknowledgement) and represents a finer sampling at $l = 11$ periods and represents one map each for Love and Rayleigh phase and group dispersion maps for a total of forty-four maps $2 \times 2 \times 11 = 44$ .We present a summary of the ensemble statistics for the entire solution in Tables 2 & 3. This summary provides a synthesis of the posterior distribution for the entire set of dispersion maps, providing insights into which regions in Africa are best resolved; that is, which regions captured by all the dispersion maps are constrained with high precision and are not biased towards unreasonably large or small velocities. Finally, we produce illustrative examples of the new model of Africa's crustal shear-velocity model using ADAMA's Rayleigh wave phase maps and uncertainties as constraints (ACE-ADAMA-RP).

4.1 THBI Solutions: Exemplary Phase Maps with Errors

The rj-McMC algorithm is run on ~ 20 parallel chains for a total of 1 million iterations. For each Markov chain, accepted model ensembles are downsampled every 100 steps, and the final average and standard deviation are computed to produce final maps of Love and Rayleigh wave dispersion maps. We downsample, or "thin", the model ensemble to avoid potential biases from interdependence (Bodin et al., 2009; T. M. Olugboji et al., 2017). We show exemplary maps at four distinct periods, from the shortest to longest periods (Figures 5 & 6). Dispersion maps display spatial heterogeneity that depends on wavelength: more heterogeneity at shorter periods than long periods.

Prior Distributions Min cell (200) Max cell (2000) initial cell (320) Min group sigma (1) Max group sigma (45)								
	Rayleigh				Love			
	σ_i		$\bar{C}^R$		σ_i		$\bar{C}^L$	
T	MIN	MAX	MIN	MAX	MIN	MAX	MIN	MAX
5	12	45	0.2	6	12	45	0.2	6
6	1	45	0.2	5.5	1	45	0.2	6
8	1	45	0.2	6	1	45	0.2	6
10	1	25	0.5	6	10	45	0.2	5.5
12	1	40	0.2	6	1	40	0.2	6
15	1	40	1	6	1	40	1	6
20	1	40	0.5	6	1	40	0.5	6
25	1	30	0.5	6	1	30	0.5	6
30	1	30	0.5	6	1	30	0.5	6
35	1	25	1	6	1	25	1	6
40	1	20	1.5	6.5	1	20	1	6.5

	Posterior Distributions			
	Rayleigh		Love	
T	$\bar{N}_i$	$\bar{C}^R$	$\bar{N}_i$	$\bar{C}^L$
5	582	3.73	248*	3.92*
6	437	3.63	258	3.98
8	452	3.74	331	3.99
10	310	3.75	216	3.93
12	327	3.73	286	4.05
15	433	3.73	393	4.11
20	401	3.81	673	4.16
25	403	3.91	359*	4.21*
30	374	4.00	468	4.30
35	321	4.05	322	4.36
40	334	4.14	388	4.44

** : not fully converged*

Table 2. Phase Velocities.

At the shortest periods (< 12 second) we observe faster velocities in west and central Africa than in east and southern Africa (Figures a1-d1). Similar patterns of heterogeneity are observed for Love as well as Rayleigh dispersion except that Love waves travel faster than Rayleigh waves and are more sensitive to shallow structure (compare Figures 4b to Figures 2c). This explains why the Love wave maps are more heterogeneous and more uncertain than the corresponding Rayleigh maps (compare Figures 6b1 & 5b1 and Figures 6b2 & 5b2).

In general, the error maps show that the standard deviations are lowest at the longest periods (long wavelength image > 20 secs) and when data coverage is the highest (south

Prior Distributions					Posterior Distributions			
	Rayleigh		Love		Rayleigh		Love	
	U_i		U_i		$\bar{N}_i$	U_i	$\bar{N}_i$	U_i
T	MIN	MAX	MIN	MAX	-	-	-	-
5	0.2	5.5	0.2	5.5	306	3.61	308	3.66
6	0.2	5.5	0.2	6	284	3.64	431	3.83
8	0.2	5.8	0.2	6	361	3.69	374	3.86
10	0.5	6	0.2	6	776	3.68	400	3.86
12	0.5	6.2	0.5	6.2	358	3.70	279	3.92
15	1	6.5	0.5	6.5	540	3.68	334	3.97
20	1.5	6.5	1.5	7	600	3.54	571	3.98
25	1.5	7	1.5	7	690	3.61	703	3.99
30	2	7	1.5	7	389	3.72	711	4.07
35	2	7.5	2	7.5	434	3.86	414	4.17
40	2	7.5	2	8	455	3.94	618	4.29

Table 3. Group Velocities.

east vs. west and central Africa). This pattern of high uncertainties is replicated with our synthetic tests (Figure S1). We observe that the uncertainties are highest for checkerboard models and when data coverage is poor, compared to long-wavelength toy models with good data coverage. These results suggest that the THBI algorithm can appropriately model uncertainties inherent in the measurement errors as well as those inherent in the reconstruction process. Although the synthetic tests show that the greatest uncertainties should be expected where the station coverage is sparse, a few more statistically significant patterns are distinguishable in our results, even for poor data coverage regions e.g., along the Congo craton (compares Figures 5 & 6 with Figures 2a). We use the full statistics of the posterior distributions to explore these patterns and describe regions of our maps that are resolved with high-precision. This is important for judging final crustal model updates.

4.2 Ensemble Statistics of Noise Maps: Convergence & Posterior Distributions

As we've pointed out, the spatial distribution of the standard-deviation (error maps) is fundamentally governed by measurement error, as well as raypath sampling. As a result, we observe that the Rayleigh maps are better resolved than the Love maps, with the noisiest maps being observed at the shortest periods. This is not surprising, since horizontally polarized waves are noisier at this period. We also observe that the most problematic maps are the 6 and 10 second maps . We summarize the statistical property of the maps across different periods by classifying each pixel in Africa based on: (1) its standard deviations and (2) the amplitude of the absolute velocity relative to a 1-D reference model (ak135). At each location, the dispersion maps are either precise or biased depending on these two measures. For example, a phase dispersion at a particular pixel location is recovered with high precision and low bias when no more than two discrete periods have standard deviations that exceed 0.4 km/s and the phase velocity values are not biased towards unreasonably high values ($>$ 40% of the reference value). Based on this scheme, we classify our entire domain into four categories: (1) High precision, (2) Low precision, (3) Biased, (4) Unbiased,

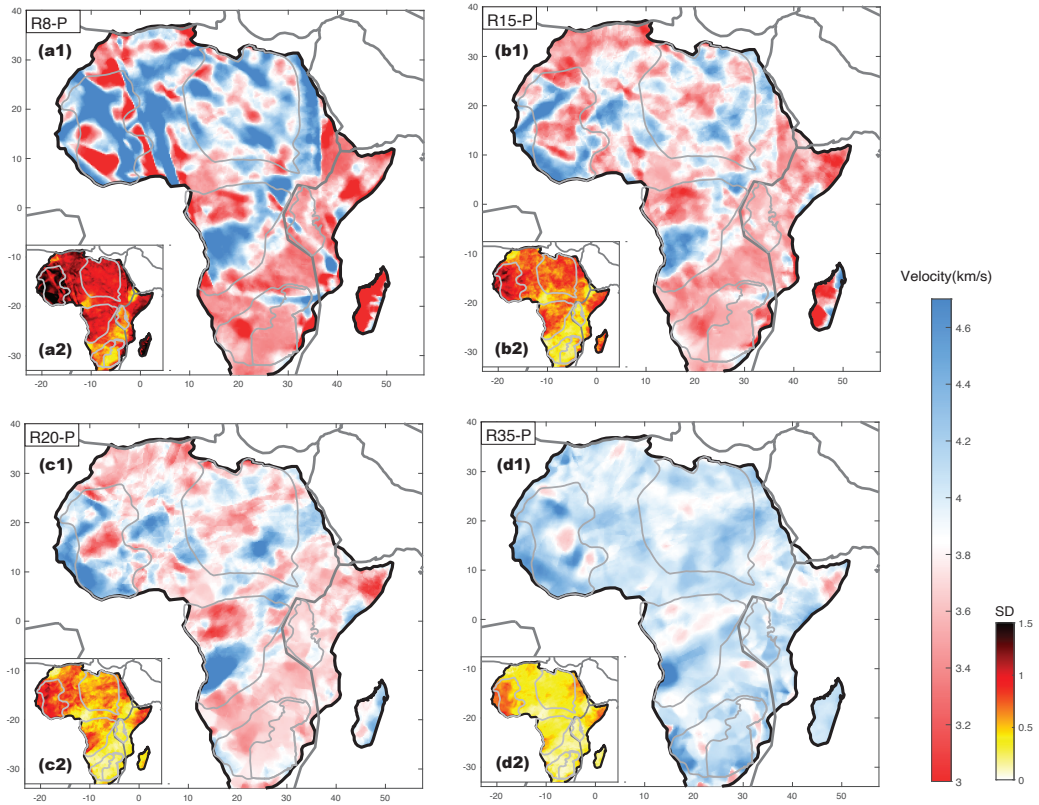

Figure 5. Rayleigh-wave phase maps and associated uncertainties at four discrete periods constructed using THBI. (a1,b1,c1,d1) Average maps constructed using the posterior distributions. (a2,b2,c2,d2) the standard deviation maps constructed using a method similar to Figure 4c. For Rayleigh wave group velocity maps see Figure S2.

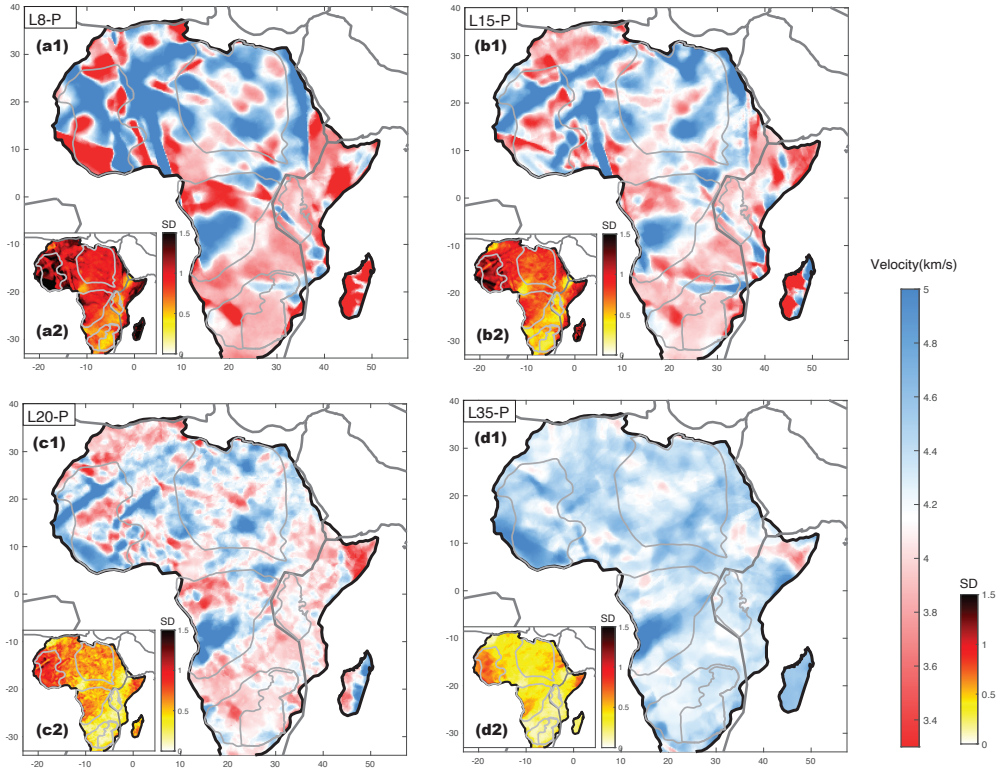

Figure 6. Same as Figure 5 but for Love-wave phase dispersion. For group velocity maps see Figure S3.

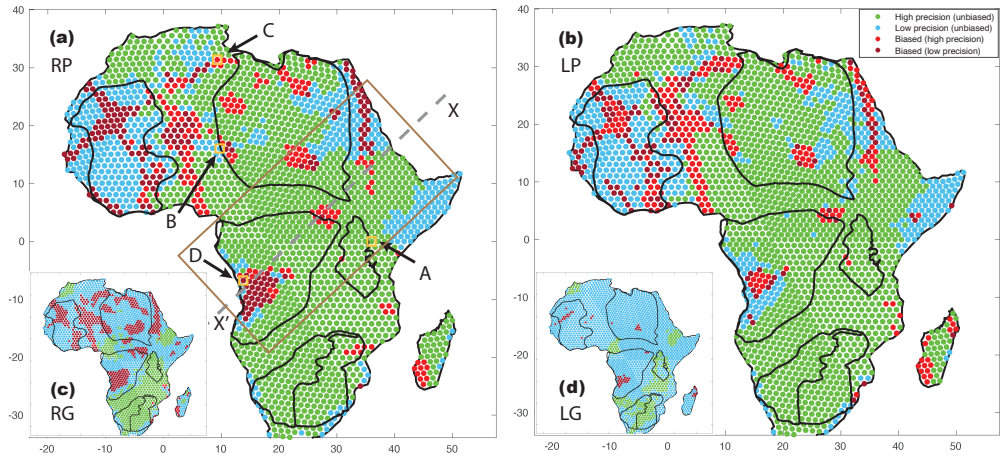

Figure 7. The quality of Rayleigh and Love dispersion models derived based on ensemble statistics. (a) The spatial statistics of Rayleigh phase dispersion is color-coded by precision and bias: high precision and unbiased (green), low precision and unbiased (blue) high-precision and biased (red), low precision and biased (brown). We identify four locations (A-B-C-D) that exemplify these four classes (b) The spatial statistics of Love phase dispersion (c) The spatial statistics of Rayleigh group dispersion (d) The spatial statistics of Love group dispersion. Model update and assessment using Rayleigh phase dispersion curves and associated uncertainties are shown at the four locations (Figure 8) and on a transect X'X crossing south-west to North-east (Figure 9).

each reflecting broad statistics (Figure 7). This is a comprehensive way to summarize the uncertainty inherent in our THBI solutions and how they are propagated onwards into the model update of Africa's crust.

We observe only a slight difference in Rayleigh and Love phase dispersion precision and bias: 64.4%, by area, for Rayleigh and 63.3%, by area, for Love. In particular, regions like Madagascar, the Sahara metacraton, the cratons of southern, central, and eastern Africa and the atlas mountains of North Africa are recovered with high precision and low bias (green dots of Figures 7a & 7b). While these regions are recovered with a high precision, some portions are highly biased. For example, the west-end of the Congo craton and the eastern edge of the Sahara meta craton. Within this large sea of 'high precision-low-bias' regions are regions on the east with low-precision-low-bias: the Horn of Africa and the western African craton (blue dots of Figures 7a & 7b). The western African craton also has the most regions with very highly biased dispersion curves (red dots of Figure 7). Again, these broad patterns are well explained by comparison with the spatial patterns of raypath coverage. Regions with the lowest precision and that are highly biased often intersect with regions of very low ray path coverage – for example, the western Africa craton, the Horn of Africa, and the eastern edge of the Congo craton (see Figure 2a).

Compared to the phase dispersion maps, the group dispersion maps have larger uncertainties, with only 25.3% and 13.5% by area of Rayleigh, and Love, being recovered with high precision, with large portions being recovered with very low precision and high bias (Figure 7c & 7d). While this makes it difficult to use the group dispersion results for continent-wide model assessment or update, we observe improvements in precision at some specific regions, made possible by short-aperture, country-wide seismic array deployments in Morocco, Cameroon, Ethiopia, Tanzania, and Southern Africa (T. Olugboji & Xue, 2022). For example, the cratons in the east and south of Africa are the best resolved as well as the highlands of Ethiopia, Morocco and the volcanic regions of Cameroon (compare 7c & 7d with Figure 1b). Next, the group dispersion maps for Congo craton and Sahara metacraton are moderately well resolved with only a few regions with highly biased values with low-precision (the western edge of the Congo craton, and a few regions in the Sahara meta craton). Finally, we observe the worst resolution for the west African craton and the mobile belts between the west african and sahara metacraton. While the group dispersion maps are not currently used in the model update, other authors may elect to use it as a constraint for investigating targeted regional crustal structure especially in highly resolved regions. For completeness, we report the entire dataset and provide the digital maps as a reference. In general, the spatial statistics of our dispersion maps shows that continent-wide model updates, using Rayleigh wave phase dispersion, are statistically significant, with room for improvement in low-resolution regions (blue and red dots of Figure 7a).

4.3 Africa's Crustal Structure: Model Update and Assessment of Shear-wave Velocity

To complete our analysis, we present a new continent-wide, shear-wave crustal velocity model of the entire African continent using the Rayleigh wave phase dispersion maps and uncertainties as a data constraint. The decision to use this dispersion dataset is predicated upon the error statistics presented in the previous section (Figure 7). An attempt to use both phase and group dispersion would lead to a final crustal model that inherits a larger set of biased and unreliable dispersion curves (Figures 7c & 7d). The new model is constructed using the Litho1.0 model as a reference starting model, therefore, we consider it both a model update as well as a model assessment product of the crust within Africa. An inversion at each grid point produces an updated 1-D model (Figure 8) that is interpolated into a quasi-3D shear velocity model which we visualize by taking 2-D vertical and horizontal projections at selected transects and depth-slices across the entire model domain. We show a few such examples selected to highlight geographic regions and crustal depths where we expect to see improvements in resolution based on better ray-path coverage and improved resolution from our short-period ADAMA catalog (Figure 2b). The 2-D projections include: (1) a vertical slice defined by a transect that runs from the western edge of the Congo craton on towards.

Ethiopia (Figures. 7a & 9) and (2) four horizontal slices spaced at 10-km intervals starting at the topmost crust and terminating around the Moho which is at 40 km for most of Africa (Figure 10). The vertical slice through our updated crustal model illustrates the utility of ensemble statistics. The shear-velocities are typically left unchanged when ADAMA's Rayleigh dispersion curves do not statistically differ significantly from that of the starting reference model. Significant model updates are observed within the topmost crust (Figure 9a) informed by improved resolution at the shortest periods (Figure 2c). The updated crustal velocity model also includes uncertainties that have been forward propagated from the McMC ensemble (Figure S4b). This shows that not all regions of our model update are equally well resolved. For example, along transect X'X, the shallow crust underneath the Angolan and Bomu-Kibalan shields are the least resolved with higher standard deviations and highly biased velocities (compare Figure 7a and Figure S4b). This point is further elaborated by the four horizontal slices across the model update, ACE-ADAMA-RP, and compared with the Litho1.0 starting reference model (Figure 10). We observe the largest differences between Litho1.0 and ACE-ADAMA-RP within the top and middle crust (¡ 20 km) especially along craton edges, with our new model tending to have higher shear

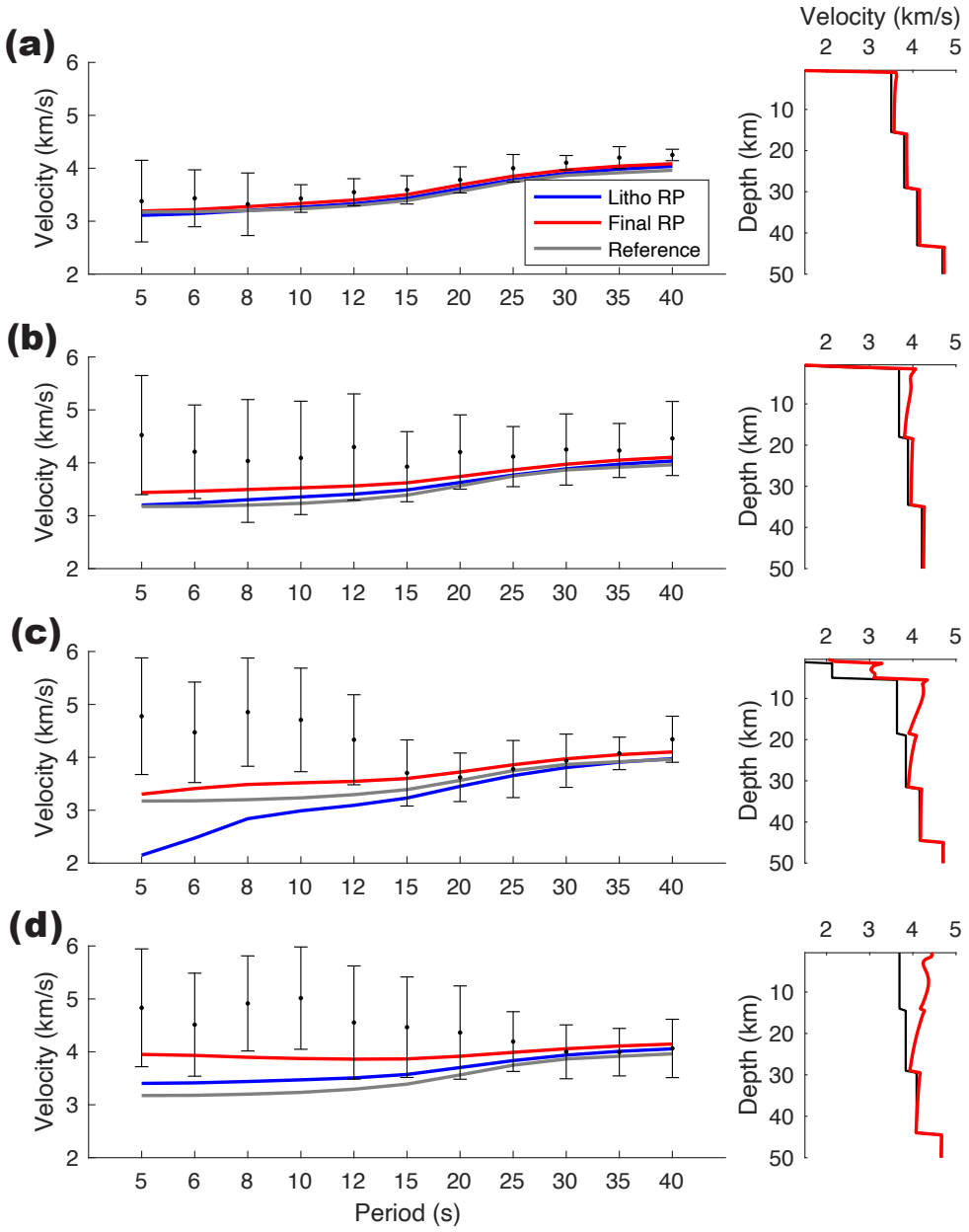

Figure 8. Illustrative examples showing model assessment and update of Litho1.0's shear-wave velocity using ADAMA's Rayleigh wave phase dispersion curve and uncertainties. Model assessment and update for: (a) a high precision and unbiased dispersion curve, starting phase velocity from Litho1.0 model (blue curve), final dispersion curve after the perturbational inversion scheme described in section 3.3 (red line) (b) a low precision and unbiased dispersion data (c) a biased and low precision data (d) a biased and high precision data. For a plot of the other predictions see Figure S2. The locations of the examples in a-d above are shown in the right map.

velocities compared to Litho1.0. Within the interiors of the Congo Craton and the Sahara Meta Craton new features are recovered that are absent in Litho1.0. For example, the high-velocity domains in the eastern edge of the Congo craton and within the North and eastern end of the Sahara Meta Craton (Figure 10a-10c).

While some of these features are recovered from the least resolved dispersion curves (high-velocity western boundaries of the western African and Congo craton), they cannot be entirely explained by poor measurements since they are spatially coherent across the entire crust and can be seen at the longest periods in both the Rayleigh and Love dispersion measurements, which are recovered with better resolution (compare for example Figure 7 with Figures 4-6). The spatial extent and the reliability of these features may require further tests as improvements in station coverage and data quality lead to improvements in spatial resolution and lead to more precise dispersion maps.

5 Discussion and Interpretation

We have constructed a continent-wide shear velocity model of the entire African continent and Madagascar using a probabilistic and perturbational inversion of the most comprehensive ambient noise dispersion measurements to date (T. Olugboji & Xue, 2022). This work, in Africa, is similar to other continent-wide studies that produce crustal seismic models based on short period passive source ambient noise seismic data (Saygin & Kennett, 2012; Shen et al., 2012; Lu et al., 2018). However, in our study, we have applied the probabilistic approach to constructing the ambient noise dispersion maps (Zulfakriza et al., 2014; Galetti et al., 2016; Yuan & Bodin, 2018; Eshetu et al., 2021). The statistical inference facilitated by a probabilistic approach has allowed us to pose, and answer, fundamental questions about the statistical significance of our new dispersion results and how they inform model updates of Africa's crust (T. M. Olugboji et al., 2017): (1) at which periods are the dispersion maps best resolved? (2) which regions of Africa need significant updates, and which do not? (3) In the regions with improved resolution, and requiring significant model updates, to what degree do existing reference models differ from current model updates based on the most precise dispersion measurements i.e., Rayleigh wave phase dispersion data? Our current update of Africa's Crust (ACE-ADAMA-RP) answers all these questions, and extends our understanding of Africa's crustal architecture compared to existing ambient-noise crustal models (Pasyanos et al., 2014; Emry et al., 2019; Ojo et al., 2020).

We reiterate that the model we have constructed here is informed primarily by the vertically polarized ambient noise dispersion maps alone, and future work will explore other passive source datasets like receiver functions, earthquake surface wave tomography, and other seismic observables that extend resolution in the lithosphere from the crust into the upper mantle (Shen et al., 2012, 2018; Gao et al., 2022; Han et al., 2022). We anticipate that such future model updates will extend lateral resolution only if new datasets are collected primarily in regions with the poor spatial resolution, e.g. western Africa craton (Figure 7). When incorporating other passive source datasets, the improved depth resolution of other elastic-properties like compressional wave speed, poisson ratio, are expected only when new seismic deployments overlap with low-resolution regions. For seismic methods, like receiver functions, that improve sensitivity right underneath the seismic station then depth resolution of crust and mantle discontinuities will only be possible when stations are co-located with regions with high resolution from surface wave studies. In what follows, we review the current state of seismic models of the crust (Begg et al., 2009; Crosby et al., 2010; Raveloson et al., 2015; Finger et al., 2022), we contrast this with Moho models based on joint inversion with other geophysical methods of obtain thermo-compositional models of the African lithosphere (Globig et al., 2016; Raveloson et al., 2021; Haas et al., 2021; Afonso et al., 2022).

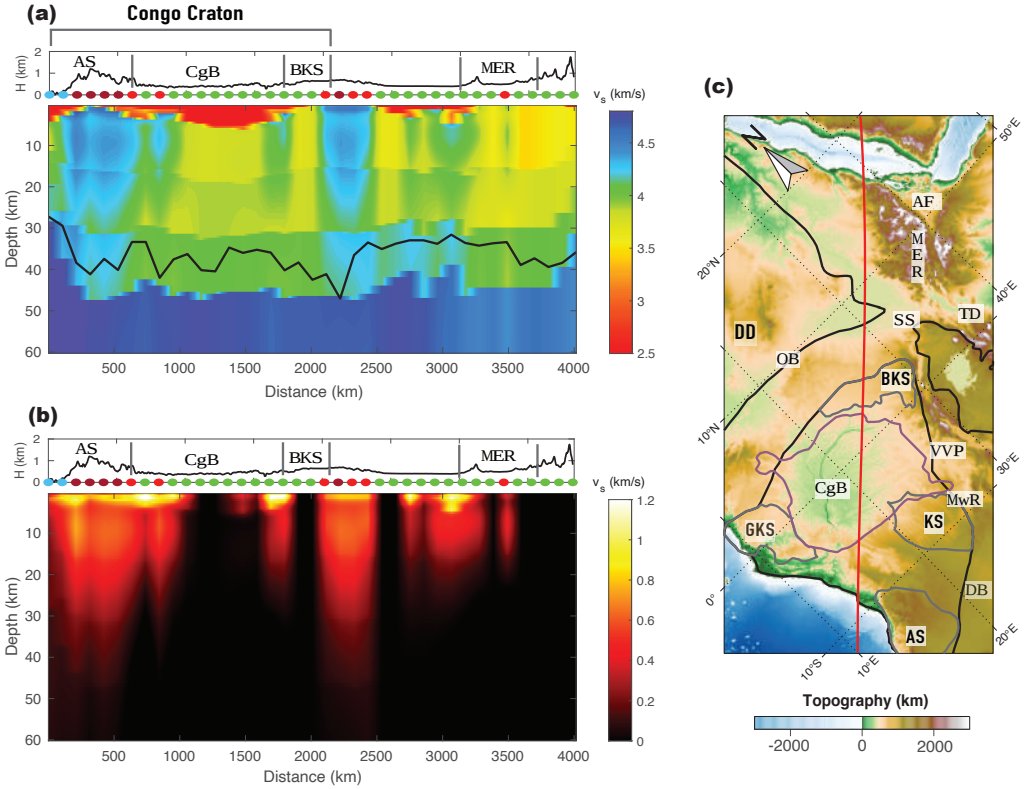

Figure 9. A vertical slice through, ACE-ADAMA-RP, the updated shear-velocity model of Africa's Crust based on ADAMA's Rayleigh wave phase dispersion curves. (a) The shear velocity model through transect X'X starts from the western edge of the Congo craton on towards Ethiopia (see Figure 7a). The depth to the crust-mantle boundary is shown for reference and taken from (Globig et al., 2016). (b) The difference between the final model and the starting model. (Top of 9a & 9b) Topography running through transect X'X with abbreviations same as in Figure 1a and statistical properties of each region (colored circles) same as in Figure 7a. (c) The geology surrounding transect X'X showing domains within the Congo craton, continental shield domains, the congo basin, and surrounding areas. The outline of the Congo basin is taken from (Andriamiranto Raveloson et al. 2015; A. Raveloson et al. 2021). For a view of the starting model used for the update and standard deviation of the final shear-velocity model see Figure S4a & S4b

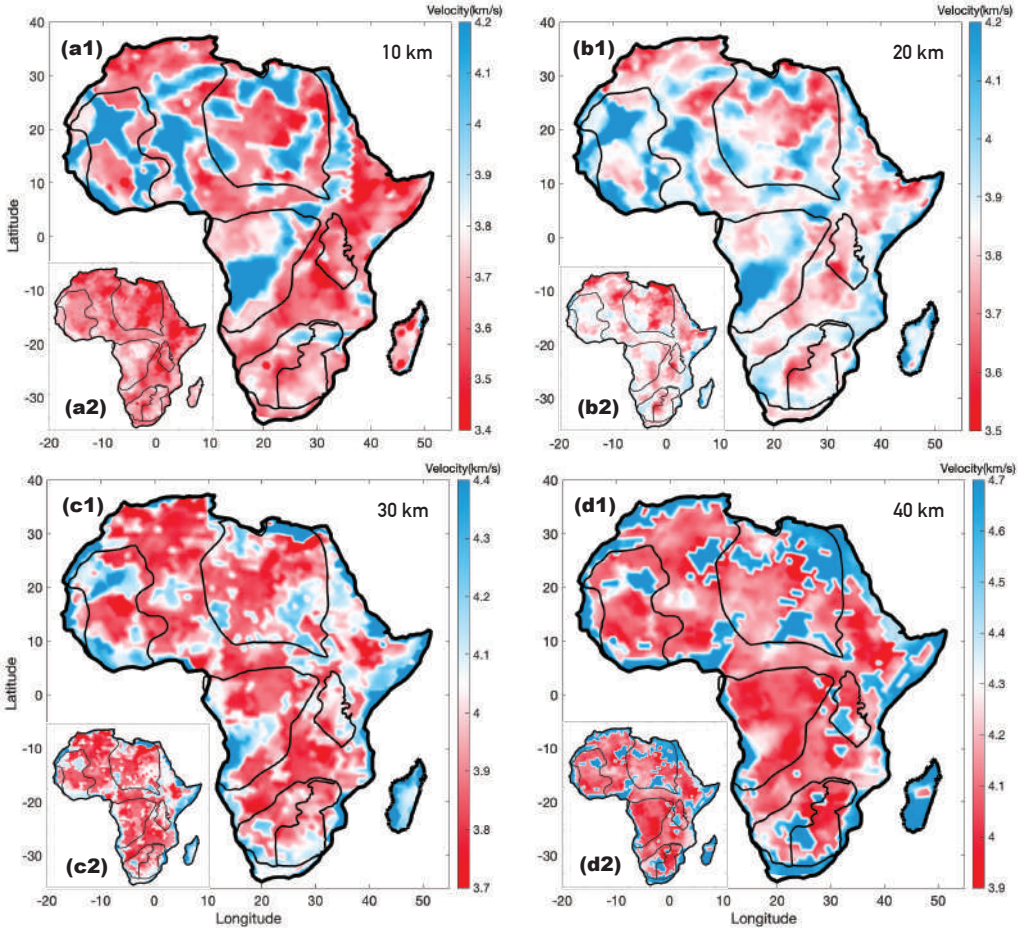

Figure 10. Horizontal slices through the updated shear-velocity model of Africa's crust. Recovered shear velocity at (a) Crustal depth of 10-km compared to Litho1.0 (b) Crustal depth of 20-km and compared to Litho1.0 (c) Crustal depth of 30-km (d) Moho and Sub-crustal depth of 40 km. All horizontal slices through the starting model of Litho1.0 are taken at the same depth as the new updated model. The transect X'X is included for reference.

5.1 Comparing ADAMA to other Ambient Noise Models of Africa's Crust

A few previous studies have used ambient noise measurements to construct regional and continent-wide seismic velocity models on the continent (Yang et al., 2008; Kim et al., 2012; Pasyanos et al., 2014; Accardo et al., 2017; Borrego et al., 2018; Emry et al., 2019; Fadel et al., 2020; White-Gaynor et al., 2021). Only two of these extend across the continent providing complete crustal imaging of Africa (Pasyanos et al., 2014; Emry et al., 2019). Both studies use fewer stations and calculate dispersion measurements at periods >30 secs, therefore limiting their spatial resolution to long-wavelength features and their depth resolution to the lowermost crust and sub-moho depths (>33 km). By comparison, our work extends the resolution of crustal structure both laterally and at depth, since we extend these use a large catalog of shortest periods: 25 - 5 secs (Figure 2b) (T. Olugboji & Xue, 2022). Similar regional models (Kim et al., 2012; Borrego et al., 2018; Chambers et al., 2019; Wang et al., 2019; Fadel et al., 2020; Eshetu et al., 2021; White-Gaynor et al., 2021; Malory et al., 2022) do a similar job at providing improved depth and spatial resolution, but they do not allow a complete view of the continent-scale features. Unlike all the other models, however, the probabilistic approach makes it possible to use the large-ensemble statistics to judge resolvability of various features on the continent.

We point out that not all the features in our crustal model are well resolved. This is because of the uncertainties inherited from the dispersion measurements. While this might at first be discouraging, we note that we are able to identify and quantify the total area of the entire continent that is not well resolved (Figure 7). All in all, this provides users of our new velocity models with a quantitative judgment of how much confidence to place in the various parts of our new model update and which regions are highest priorities for continued updates as new seismic measurements are assimilated. As an example, it is clear that major updates are still required for the western African craton since only a few dispersion measurements have been made in that region of the African continent. Also, compared to the phase dispersion, the group dispersion measurements are still only useful for regional updates of the African continental crust (cf Figure 7b & 7c). We expect that future targets will include constraining radial anisotropy (Lin et al., 2010; Moschetti et al., 2010a, 2010b; Ojo et al., 2017) along regions where both Rayleigh and Love dispersion measurements are highly resolved with high precision, e.g., eastern and Southernmost Africa.

5.2 ACE-ADAMA compared to other Geophysical Constraints on Africa's Crustal Structure

Compared to other regions or the world, Africa is sparsely instrumented and therefore earlier seismic models based on combined active and passive source seismics have required extensive spatial averaging (Mooney, 2010; Fishwick & Bastow, 2011; Stolk et al., 2013; Globig et al., 2016). These are heavily spatially aliased models of the bulk velocity in the crust or it's thickness (Moho depth) and have been conducted using several techniques that can be broadly categorized into three categories: (1) passive source seismics with sensitivity to the crust, e.g., receiver functions, ambient noise, or SS reflectivity (Pasyanos & Nyblade, 2007; Rychert & Shearer, 2010; Tugume et al., 2013; Globig et al., 2016) (2) regionalized earthquake body wave tomography models with only marginal sensitivity to the crust, (Celli, Lebedev, Schaeffer, & Gaina, 2020; Boyce et al., 2021), and (3) joint gravity and seismic models (Haas et al., 2021; Finger et al., 2021, 2022). Compared to these techniques, we provide the best resolution on the bulk shear velocity in the crust. This is because our dataset includes an extensive measurement comprising small aperture regional networks (Nyblade, 2015; Fadel et al., 2018; Yu et al., 2020; T. Olugboji & Xue, 2022) and the adaptive probabilistic tomography approach based on these high-resolution ambient noise surface wave data improves resolution of the bulk velocities without imposing strict limiting assumptions on spatial averaging or smoothness (Bodin, Sambridge, Rawlinson, & Arroucau, 2012; Sambridge et al., 2013; Belhadj et al., 2018).

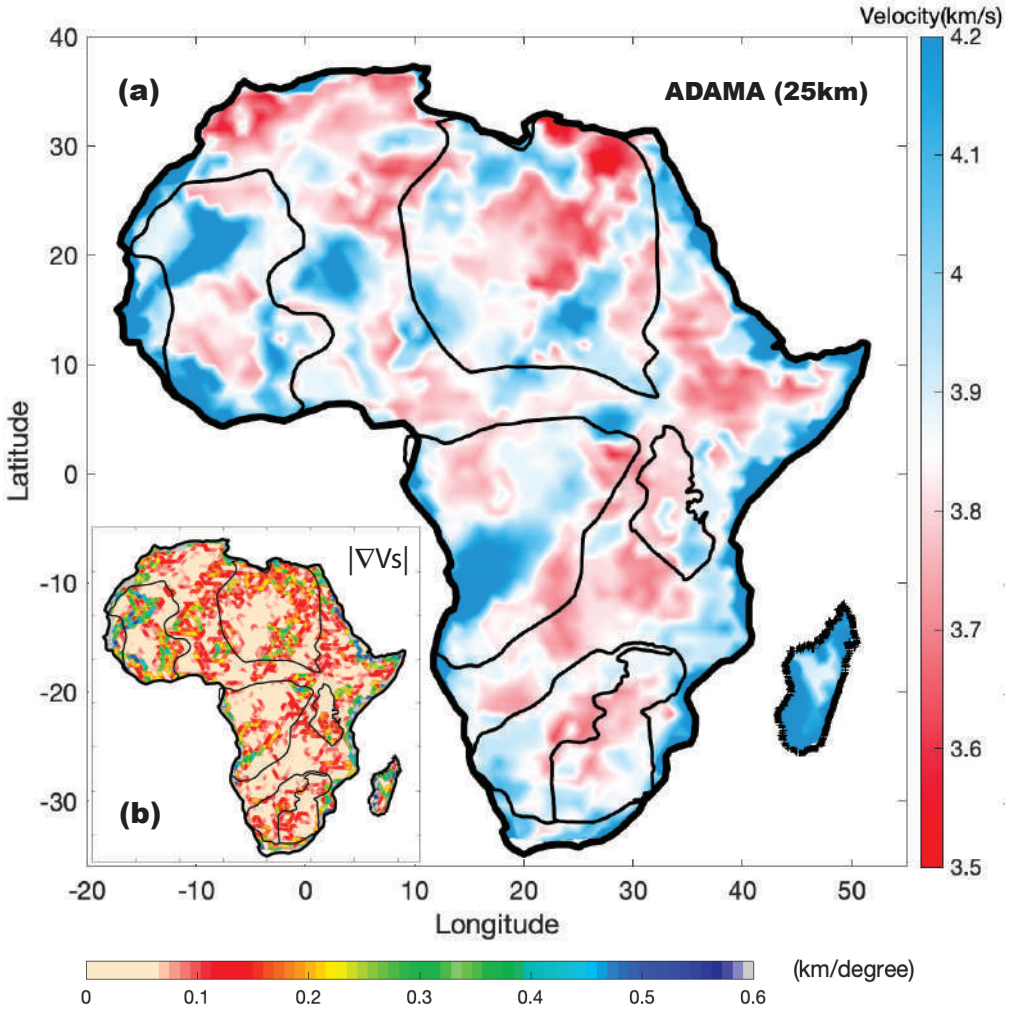

Figure 11. A view of the shear-wave velocity and its lateral gradients through the lowermost crust of Africa and Madagascar as seen by the ACE-ADAMA-RP model update. (a) The continent-wide shear wave velocities at 25 km in Africa and Madagascar. (b) The spatial gradient of the velocity field shown in (a) highlighting the regions with greatest lateral changes in shear velocities: continental margins, craton edges, and the mobile belts between WAC and SMC

5.3 Newly Resolved Features & Future Application of new Continent-wide Model

As an illustrative example of some of the newly resolved features in our new shear velocity model, we show a horizontal depth at 25 km (Figure 11). This portion of our model is constrained by highly precise Rayleigh wave dispersion measurements between 20 seconds and 35 seconds (Figures 2b, 5c2, and 4d2) and therefore the newly resolved features can be interpreted with better confidence. Compared with the reference model, Litho1.0, the shear-wave velocities are faster within the exposed Archean shields, along the continental margins, and especially for a few of the craton edges (compare Figure 10b2 with Figure 11). In particular the outlines of the Archean shields in the west African craton and the Congo craton are much more prominent and almost follow outlines predicted by the surface geology (Begg et al., 2009). The spatial homogeneity of some of these features are clearly seen in the image of the lateral gradient were the velocities hardly vary except at the edges of the shields, at the continental margins and in the highly mobile belts of between the west African craton and the sahara Meta Craton. While these are some preliminary interpretations of the connections between the surface geology and crustal architecture revealed by our new model, we expect that future work will explore application to other geological and geophysical problems, e.g., improving constraining crustal composition (Hacker et al., 2012; Sammon et al., 2021; Sammon & McDonough, 2021; Afonso et al., 2022), lithospheric stress modeling (Zoback & Mooney, 2003; Stamps et al., 2010; Craig et al., 2011), and connection to long-term deformation and seismicity on the African continent (Schmandt et al., 2015; Fadel et al., 2020).

6 Conclusion

We construct a new shear-wave velocity model of Africa's crustal architecture using a probabilistic and perturbational inversion of ambient noise surface wave measurements. The probabilistic inversion solves for phase and group dispersion maps using a transdimensional and hierarchical Bayesian inversion of a large catalog of interstation dispersion data. The dispersion map solutions are large ensemble models of a posterior distribution and provide estimates of statistical significance. An evaluation of the error statistics suggests that the phase dispersion is better constrained than group dispersion, with Rayleigh wave phase dispersion maps possessing the best resolution. Informed by these error statistics, we use a perturbational approach to construct the updated model of Africa's crustal architecture evaluated using the Rayleigh phase maps and starting from a reference global model (Litho 1.0). The model recovers new features not present in existing maps, with important implications for crustal structure and geological architecture of Archean cratons, exposed shields and mobile belts within Africa.

7 Data Availability Statement

No seismic data was used in this study. The full catalog of dispersion measurements can be obtained from (Xue Olugboji 2021) and was published alongside (T. Olugboji & Xue, 2022). A digital format of the probabilistic surface wave dispersion maps and the shear velocity model of Africa's Crust Evaluated using the ADAMA Rayleigh wave Phase dispersion (ACE-ADAMA-RP) is available at doi: 10.5281/zenodo.8017840.

8 Acknowledgements

This work was made possible by the National Science Foundation under grant number: 2102495. We thank the Incorporated Research Institutions for Seismology (IRIS), whose internship program allowed Tamama to pursue this research We thank Siyu Xue, for computing the ambient noise cross correlations for all station pairs and providing us with the Love and Rayleigh wave dispersion measurements crucial to this project. We thank Baowei

Liu for his assistance in preparing our inversions. We thank the University of Rochester's Center for Integrated Research Computing (CIRC), for providing us with the computational support and resources for this project. We also thank Carl Schmidtman and Miki Nakajima for generously allocating us with additional computational resources. We acknowledge many helpful discussions with Lara Wagner, Baowei Liu, Ziqi Zhang, Canberk Eckmecki.

References

Accardo, N. J., Gaherty, J. B., Shillington, D. J., Ebinger, C. J., Nyblade, A. A., Mbogoni, G. J., ... Mruma, A. (2017, June). Surface wave imaging of the weakly extended malawi rift from ambient-noise and teleseismic rayleigh waves from onshore and lake-bottom seismometers. *Geophys. J. Int.*, *209*(3), 1892–1905.

Adams, A., & Nyblade, A. (2011, August). Shear wave velocity structure of the southern african upper mantle with implications for the uplift of southern africa. *Geophys. J. Int.*, *186*(2), 808–824.

Afonso, J. C., Ben-Mansour, W., O'Reilly, S. Y., Griffin, W. L., Salajeghegh, F., Foley, S., ... Yang, Y. (2022, April). Thermochemical structure and evolution of cratonic lithosphere in central and southern africa. *Nat. Geosci.*, *15*(5), 405–410.

Begg, G. C., Griffin, W. L., Natapov, L. M., O'Reilly, S. Y., Grand, S. P., O'Neill, C. J., ... Bowden, P. (2009, February). The lithospheric architecture of africa: Seismic tomography, mantle petrology, and tectonic evolution. *Geosphere*, *5*(1), 23–50.

Behn, M. D., Lin, J., & Zuber, M. T. (2002, September). A continuum mechanics model for normal faulting using a strain-rate softening rheology: implications for thermal and rheological controls on continental and oceanic rifting. *Earth Planet. Sci. Lett.*, *202*(3), 725–740.

Belhadj, J., Romary, T., Gesret, A., Noble, M., & Figliuzzi, B. (2018, May). New parameterizations for bayesian seismic tomography. *Inverse Probl.*, *34*(6), 065007.

Bodin, T., & Sambridge, M. (2009, September). Seismic tomography with the reversible jump algorithm. *Geophys. J. Int.*, *178*(3), 1411–1436.

Bodin, T., Sambridge, M., & Gallagher, K. (2009, March). A self-parametrizing partition model approach to tomographic inverse problems. *Inverse Probl.*, *25*(5), 055009.

Bodin, T., Sambridge, M., Rawlinson, N., & Arroucau, P. (2012, June). Transdimensional tomography with unknown data noise. *Geophys. J. Int.*, *189*(3), 1536–1556.

Bodin, T., Sambridge, M., Tkalčić, H., Arroucau, P., Gallagher, K., & Rawlinson, N. (2012). Transdimensional inversion of receiver functions and surface wave dispersion. *J. Geophys. Res. [Solid Earth]*, *117*(B2).

Borrego, D., Nyblade, A. A., Accardo, N. J., & others. (2018). Crustal structure surrounding the northern malawi rift and beneath the rungwe volcanic province, east africa. *Geophys. J*.

Boyce, A., Bastow, I. D., Cottaar, S., Kounoudis, R., Guilloud De Courbeville, J., Caunt, E., & Desai, S. (2021, March). AFRP20: New P -wavespeed model for the african mantle reveals two whole-mantle plumes below east africa and neoproterozoic modification of the tanzania craton. *Geochem. Geophys. Geosyst.*, *22*(3).

Brocher, T. M. (2005). Empirical relations between elastic wavespeeds and density in the earth's crust. *Bull. Seismol. Soc. Am.*, *95*(6), 2081–2092.

Buehler, J. S., & Shearer, P. M. (2017). Uppermost mantle seismic velocity structure beneath USArray. *J. Geophys. Res. [Solid Earth]*, *122*(1), 436–448.

Burke, K., & Gunnell, Y. (2008, January). The african erosion surface: A Continental-Scale synthesis of geomorphology, tectonics, and environmental. In *Memoir 201: The african erosion surface: A Continental-Scale synthesis of geomorphology, tectonics, and environmental change over the past 180 million years* (Vol. 201, pp. 1–66). Geological Society of America.

Celli, N. L., Lebedev, S., Schaeffer, A. J., & Gaina, C. (2020, January). African cratonic lithosphere carved by mantle plumes. *Nat. Commun.*, *11*(1), 92.

Celli, N. L., Lebedev, S., Schaeffer, A. J., Ravenna, M., & Gaina, C. (2020, April). The upper mantle beneath the south atlantic ocean, south america and africa from waveform tomography with massive data sets. *Geophys. J. Int.*, *221*(1), 178–204.

Chambers, E. L., Harmon, N., Keir, D., & Rychert, C. A. (2019, April). Using ambient noise to image the northern east african rift. *Geochem. Geophys. Geosyst.*, *20*(4), 2091–2109.

Chorowicz, J. (2005, October). The east african rift system. *J. Afr. Earth. Sci.*, *43*(1), 379–410.

Craig, T. J., Jackson, J. A., Priestley, K., & McKenzie, D. (2011, April). Earthquake distribution patterns in africa: their relationship to variations in lithospheric and geological structure, and their rheological implications. *Geophys. J. Int.*, *185*(1), 403–434.

Crosby, A. G., Fishwick, S., & White, N. (2010, June). Structure and evolution of the intracratonic congo basin. *Geochem. Geophys. Geosyst.*, *11*(6).

Crowder, E., Rawlinson, N., Pilia, S., Cornwell, D. G., & Reading, A. M. (2019, January). Transdimensional ambient noise tomography of bass strait, southeast australia, reveals the sedimentary basin and deep crustal structure beneath a failed continental rift. *Geophys. J. Int.*, *217*(2), 970–987.

Doucouré, C. M., & de Wit, M. J. (2003, May). Old inherited origin for the present near-bimodal topography of africa. *J. Afr. Earth. Sci.*, *36*(4), 371–388.

Emry, E. L., Shen, Y., Nyblade, A. A., Flinders, A., & Bao, X. (2019). Upper mantle earth structure in africa from Full-Wave ambient noise tomography. *Geochem. Geophys. Geosyst.*, *20*(1), 120–147.

Eshetu, A., Mammo, T., & Tilmann, F. (2021, November). Imaging the ethiopian rift region using transdimensional hierarchical seismic noise tomography. *Pure Appl. Geophys.*, *178*(11), 4367–4388.

Fadel, I., Paulssen, H., van der Meijde, M., Kwadiba, M., Ntibinyane, O., Nyblade, A., & Durrheim, R. (2020). Crustal and upper mantle shear wave velocity structure of botswana: The 3 april 2017 central botswana earthquake linked to the east african rift system. *Geophys. Res. Lett.*, *47*(4), e2019GL085598.

Fadel, I., van der Meijde, M., & Paulssen, H. (2018, December). Crustal structure and dynamics of botswana. *J. Geophys. Res. [Solid Earth]*, *123*(12), 10,659–10,671.

Finger, N.-P., Kaban, M. K., Tesauro, M., Mooney, W. D., & Thomas, M. (2021, November). *Thermo-compositional model of cratonic lithosphere and depth to moho of africa.* GFZ Data Services.

Finger, N.-P., Kaban, M. K., Tesauro, M., Mooney, W. D., & Thomas, M. (2022, March). A thermo-compositional model of the african cratonic lithosphere. *Geochem. Geophys. Geosyst.*, *23*(3).

Fishwick, S., & Bastow, I. D. (2011, January). Towards a better understanding of african topography: a review of passive-source seismic studies of the african crust and upper mantle. *Geological Society, London, Special Publications*, *357*(1), 343–371.

Galetti, E., Curtis, A., Baptie, B., Jenkins, D., & Nicolson, H. (2016, August). Transdimensional love-wave tomography of the british isles and shear-velocity structure of the east irish sea basin from ambient-noise interferometry. *Geophys. J. Int.*, *208*(1), 36–58.

Gao, L., Zhang, H., Gao, L., He, C., Xin, H., & Shen, W. (2022, February). High-resolution vs tomography of south china by joint inversion of body wave and surface wave data. *Tectonophysics*, *824*, 229228.

Globig, J., Fernàndez, M., Torne, M., Vergés, J., Robert, A., & Faccenna, C. (2016). New insights into the crust and lithospheric mantle structure of africa from elevation, geoid, and thermal analysis. *J. Geophys. Res. [Solid Earth]*, *121*(7), 5389–5424.

Haas, P., Ebbing, J., Celli, N. L., & Rey, P. F. (2021). Two-step gravity inversion reveals variable architecture of african cratons. *Front Earth Sci. Chin.*, *9*, 1240.

Haas, P., Ebbing, J., & Szwillus, W. (2020, June). Sensitivity analysis of gravity gradient inversion of the moho depth—a case example for the amazonian craton. *Geophys. J.*

Int., *221*(3), 1896–1912.

Hacker, B. R., Kelemen, P. B., & Behn, M. D. (2012). Continental lower crust. *Annu. Rev. Earth Planet. Sci.*, *43*(1), 150223150959000.

Han, S., Zhang, H., Xin, H., Shen, W., & Yao, H. (2022). USTClitho2. 0: Updated unified seismic tomography models for continental china lithosphere from joint inversion of body-wave arrival times and surface-wave dispersion data. *Seismol. Res. Lett.*, *93*(1), 201–215.

Haney, M. M., & Tsai, V. C. (2017). Perturbational and nonperturbational inversion of rayleigh-wave velocities. , *82*(3).

Haney, M. M., & Tsai, V. C. (2020, January). Perturbational and nonperturbational inversion of love-wave velocities. *Geophysics*, *85*(1), F19–F26.

Hawkins, R., Bodin, T., Sambridge, M., & others. (2019). Trans-Dimensional surface reconstruction with different classes of parameterization. *Geochem. Explor. Environ. Analy.*.

Hawkins, R., & Sambridge, M. (2019, July). An adjoint technique for estimation of interstation phase and group dispersion from ambient noise cross correlations. *Bull. Seismol. Soc. Am.*, *109*(5), 1716–1728.

Jessell, M. W., Begg, G. C., & Miller, M. S. (2016, March). The geophysical signatures of the west african craton. *Precambrian Res.*, *274*, 3–24.

Kim, S., Nyblade, A. A., Rhie, J., Baag, C.-E., & Kang, T.-S. (2012, November). Crustal s-wave velocity structure of the main ethiopian rift from ambient noise tomography. *Geophys. J. Int.*, *191*(2), 865–878.

Laske, G., Masters, G., Ma, Z., & Pasyanos, M. (2013). Update on CRUST1.0 - a 1-degree global model of earth's crust. *Geophys. Res. Abstracts*, *15*(Abstract EGU2013-2658).

Lebedev, S., Adam, J. M.-C., & Meier, T. (2013, December). Mapping the moho with seismic surface waves: A review, resolution analysis, and recommended inversion strategies. *Tectonophysics*, *609*, 377–394.

Li, A., & Burke, K. (2006). Upper mantle structure of southern africa from rayleigh wave tomography. *J. Geophys. Res. [Solid Earth]*, *111*(B10).

Lin, F.-C., Ritzwoller, M. H., & Snieder, R. (2009, June). Eikonal tomography: surface wave tomography by phase front tracking across a regional broad-band seismic array. *Geophys. J. Int.*, *177*(3), 1091–1110.

Lin, F.-C., Ritzwoller, M. H., Yang, Y., Moschetti, M. P., & Fouch, M. J. (2010, December). Complex and variable crustal and uppermost mantle seismic anisotropy in the western united states. *Nat. Geosci.*, *4*(1), 55–61.

Lithgow-Bertelloni, C., & Silver, P. G. (1998, September). Dynamic topography, plate driving forces and the african superswell. *Nature*, *395*(6699), 269–272.

Lowry, A. R., & Pérez-Gussinyé, M. (2011, March). The role of crustal quartz in controlling cordilleran deformation. *Nature*, *471*(7338), 353–357.

Lu, Y., Stehly, L., & Paul, A. (2018, May). High-resolution surface wave tomography of the european crust and uppermost mantle from ambient seismic noise. *Geophys. J. Int.*, *214*(2), 1136–1150.

Malinverno, A., & Briggs, V. A. (2004, July). Expanded uncertainty quantification in inverse problems: Hierarchical bayes and empirical bayes. *Geophysics*, *69*(4), 1005–1016.

Malory, A. O., Bao, X., & Chen, Z. (2022, January). Crustal shear wave velocity and radial anisotropy beneath southern africa from ambient noise tomography. *Tectonophysics*, *822*, 229191.

Min, G., & Hou, G. (2019). *Mechanism of the mesozoic african rift system: Paleostress field modeling* (Vol. 132).

Molinari, I., & Morelli, A. (2011, April). EPcrust: a reference crustal model for the european plate. *Geophys. J. Int.*, *185*(1), 352–364.

Mooney, W. D. (2010, January). Crust and lithospheric Structure–Global crustal structure. In *Treatise on geophysics* (Vol. 1, p. 361). unknown.

Moschetti, M. P., Ritzwoller, M. H., Lin, F., & Yang, Y. (2010b). Seismic evidence for widespread western-US deep-crustal deformation caused by extension. *Nature*,

464(7290), 885–889.

Moschetti, M. P., Ritzwoller, M. H., Lin, F.-C., & Yang, Y. (2010a). Crustal shear wave velocity structure of the western united states inferred from ambient seismic noise and earthquake data. *J. Geophys. Res.*, *115*(July), 1–20.

Nair, S. K., Gao, S. S., Liu, K. H., & Silver, P. G. (2006). Southern african crustal evolution and composition: Constraints from receiver function studies. *J. Geophys. Res. [Solid Earth]*, *111*(B2).

Nyblade, A. (2015). *Nyblade, a (2015) Africaarray-Namibia [data set].*

Ojo, A. O., Ni, S., & Li, Z. (2017). Crustal radial anisotropy beneath cameroon from ambient noise tomography. *Tectonophysics*.

Ojo, A. O., Shen, W., Ni, S., Zhao, L., Xie, J., & Kao, H. (2020, November). *Lithospheric structure of africa and surrounding regions revealed by earthquake and ambient noise surface wave tomography.*

Olugboji, T., & Xue, S. (2022). A Short-Period Surface-Wave dispersion dataset for model assessment of africa's crust: ADAMA. *Bull. Seismol. Soc. Am.*, *93*(3), 1943–1959.

Olugboji, T. M., Lekic, V., & McDonough, W. (2017). A statistical assessment of seismic models of the U.S. continental crust using bayesian inversion of ambient noise surface wave dispersion data. *Tectonics*, *36*(7), 1232–1253.

Pasyanos, M. E., Masters, T. G., Laske, G., & Ma, Z. (2014). LITHO1.0: An updated crust and lithospheric model of the earth. *J. Geophys. Res. [Solid Earth]*, *119*(3), 2153–2173.

Pasyanos, M. E., & Nyblade, A. A. (2007, November). A top to bottom lithospheric study of africa and arabia. *Tectonophysics*, *444*(1), 27–44.

Pilia, S., Jackson, J. A., Hawkins, R., Kaviani, A., & Ali, M. Y. (2020, February). The southern zagros collisional orogen: New insights from transdimensional trees inversion of seismic noise. *Geophys. Res. Lett.*, *47*(4), e2019GL086258.

Raveloson, A., Nyblade, A., & Durrheim, R. (2021, July). Joint inversion of surface wave and gravity data reveals subbasin architecture of the congo basin. *Geology*, *49*(7), 810–815.

Raveloson, A., Nyblade, A., Fishwick, S., Mangongolo, A., & Master, S. (2015). The upper mantle seismic velocity structure of South-Central africa and the seismic architecture of precambrian lithosphere beneath the congo basin. In M. J. de Wit, F. Guillocheau, & M. C. J. de Wit (Eds.), *Geology and resource potential of the congo basin* (pp. 3–18). Berlin, Heidelberg: Springer Berlin Heidelberg.

Rawlinson, N., Pilia, S., Young, M., Salmon, M., & Yang, Y. (2016, October). Crust and upper mantle structure beneath southeast australia from ambient noise and teleseismic tomography. *Tectonophysics*, *689*, 143–156.

Roux, P., Sabra, K. G., Kuperman, W. A., & Roux, A. (2005, January). Ambient noise cross correlation in free space: Theoretical approach. *J. Acoust. Soc. Am.*, *117*(1), 79–84.

Rudnick, R. L., & Gao, S. (2014). Composition of the continental crust. In *Treatise on geochemistry* (2nd ed., Vol. 4, pp. 1–51). Elsevier.

Rychert, C. a., & Shearer, P. M. (2010, March). Resolving crustal thickness using SS waveform stacks. *Geophys. J. Int.*, *180*(3), 1128–1137.

Sambridge, M., Bodin, T., Gallagher, K., & Tkalcic, H. (2013, February). Transdimensional inference in the geosciences. *Philos. Trans. A Math. Phys. Eng. Sci.*, *371*(1984), 20110547.

Sambridge, M., Braun, J., & McQueen, H. (1995, December). Geophysical parametrization and interpolation of irregular data using natural neighbours. *Geophys. J. Int.*, *122*(3), 837–857.

Sammon, L. G., & McDonough, W. F. (2021, December). A geochemical review of amphibolite, granulite, and eclogite facies lithologies: Perspectives on the deep continental crust. *J. Geophys. Res. [Solid Earth]*, *126*(12).

Sammon, L. G., Mcdonough, W. F., & Mooney, W. D. (2021, July). *The composition of the deep continental crust inferred from geochemical and geophysical data.*

Saygin, E., & Kennett, B. L. N. (2012, January). Crustal structure of australia from ambient seismic noise tomography. *J. Geophys. Res.*, *117*(B1).

Schmandt, B., Lin, F.-C., & Karlstrom, K. E. (2015, December). Distinct crustal isostasy trends east and west of the rocky mountain front. *Geophys. Res. Lett.*, *42*(23), 10,290–10,298.

Schutt, D. L., Lowry, A. R., & Buehler, J. S. (2018, March). Moho temperature and mobility of lower crust in the western united states. *Geology*, *46*(3), 219–222.

Shen, W., & Ritzwoller, M. H. (2016). *Crustal and uppermost mantle structure beneath the united states* (Vol. 121) (No. 6).

Shen, W., Ritzwoller, M. H., Kang, D., Kim, Y., Lin, F.-C., Ning, J., ... Zhou, L. (2016, April). A seismic reference model for the crust and uppermost mantle beneath china from surface wave dispersion. *Geophys. J. Int.*, *206*(2), 954–979.

Shen, W., Ritzwoller, M. H., Schulte-Pelkum, V., & Lin, F.-C. (2012). Joint inversion of surface wave dispersion and receiver functions: a bayesian Monte-Carlo approach. *Geophys. J. Int.*, *192*(2), 807–836.

Shen, W., Wiens, D. A., Anandakrishnan, S., Aster, R. C., Gerstoft, P., Bromirski, P. D., ... Winberry, J. P. (2018, September). The crust and upper mantle structure of central and west antarctica from bayesian inversion of rayleigh wave and receiver functions. *J. Geophys. Res. [Solid Earth]*, *123*(9), 7824–7849.

Shinevar, W. J., Behn, M. D., & Hirth, G. (2015, October). Compositional dependence of lower crustal viscosity. *Geophys. Res. Lett.*, *42*(20), 8333–8340.

Shinevar, W. J., Behn, M. D., Hirth, G., & Jagoutz, O. (2018, July). Inferring crustal viscosity from seismic velocity: Application to the lower crust of southern california. *Earth Planet. Sci. Lett.*, *494*, 83–91.

Stamps, D. S., Flesch, L. M., & Calais, E. (2010, October). Lithospheric buoyancy forces in africa from a thin sheet approach. *Int. J. Earth Sci.*, *99*(7), 1525–1533.

Stolk, W., Kaban, M., Beekman, F., Tesauro, M., Mooney, W. D., & Cloetingh, S. (2013, August). High resolution regional crustal models from irregularly distributed data: Application to asia and adjacent areas. *Tectonophysics*, *602*, 55–68.

Trabant, C., Hutko, A. R., Bahavar, M., Karstens, R., Ahern, T., & Aster, R. (2012, September). Data products at the IRIS DMC: Stepping stones for research and other applications. *Seismol. Res. Lett.*, *83*(5), 846–854.

Tugume, F., Nyblade, A., Julià, J., & van der Meijde, M. (2013, December). Precambrian crustal structure in africa and arabia: Evidence lacking for secular variation. *Tectonophysics*, *609*, 250–266.

Wang, T., Feng, J., Liu, K. H., & Gao, S. S. (2019, March). Crustal structure beneath the malawi and luangwa rift zones and adjacent areas from ambient noise tomography. *Gondwana Res.*, *67*, 187–198.

White-Gaynor, A. L., Nyblade, A. A., Durrheim, R. J., Raveloson, R., van der Meijde, M., Fadel, I., ... Sitali, M. (2021, April). Shear-wave velocity structure of the southern african upper mantle: Implications for craton structure and plateau uplift. *Geophys. Res. Lett.*, *48*(7).

Wipperfurth, S. A., Šrámek, O., & McDonough, W. F. (2020, February). Reference models for lithospheric geoneutrino signal. *J. Geophys. Res. [Solid Earth]*, *125*(2).

Yang, Y., Li, A., & Ritzwoller, M. H. (2008, July). Crustal and uppermost mantle structure in southern africa revealed from ambient noise and teleseismic tomography. *Geophys. J. Int.*, *174*(1), 235–248.

Yu, Y., Gao, S. S., Zhao, D., & Liu, K. H. (2020, February). Mantle structure and flow beneath an early-stage continental rift: Constraints from P wave anisotropic tomography. *Tectonics*, *39*(2).

Yuan, H., & Bodin, T. (2018, July). A probabilistic shear wave velocity model of the crust in the central west australian craton constrained by transdimensional inversion of ambient noise dispersion. *Tectonics*, *37*(7), 1994–2012.

Zhou, L., Xie, J., Shen, W., Zheng, Y., Yang, Y., Shi, H., & Ritzwoller, M. H. (2012, June). The structure of the crust and uppermost mantle beneath south china from ambient

noise and earthquake tomography. *Geophys. J. Int.*, *189*(3), 1565–1583.

Zoback, M. L., & Mooney, W. D. (2003, February). Lithospheric buoyancy and continental intraplate stresses. *Int. Geol. Rev.*, *45*(2), 95–118.

Zulfakriza, Z., Saygin, E., Cummins, P. R., Widiyantoro, S., Nugraha, A. D., Lühr, B.-G., & Bodin, T. (2014, April). Upper crustal structure of central java, indonesia, from transdimensional seismic ambient noise tomography. *Geophys. J. Int.*, *197*(1), 630–635.